Materials Science & Engineering A 624 (2015) 239–249

Contents lists available at ScienceDirect

Materials Science & Engineering A

journal homepage: www.elsevier.com/locate/msea

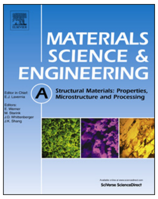

Observations of the mechanical response and evolution of damage of AA 6061-T6 under different strain rates and temperatures

A. Dorbane [a], G. Ayoub [a,b,*], B. Mansoor [a], R. Hamade [b], G. Kridli [c], A. Imad [d]

[a] Department of Mechanical Engineering, Texas A&M University at Qatar, Doha, Qatar
[b] Department of Mechanical Engineering, American University of Beirut, PO Box 11-0236 Beirut, Lebanon
[c] Center for Lightweighting Automotive Materials and Processing, University of Michigan-Dearborn, Dearborn, MI, USA
[d] Laboratoire de Mécanique de Lille, CNRS UMR 8107, Ecole Polytech'Lille, University of Lille-North of France, Cité Scientifique, Boulevard Paul Langevin, 59655 Villeneuve d'Ascq Cédex, France

ARTICLE INFO

Article history:
Received 11 September 2014
Received in revised form
13 October 2014
Accepted 22 November 2014
Available online 2 December 2014

Keywords:
AA 6061-T6
Strain rate effect
Temperature effect
Deformation mechanisms
Damage mechanisms
Failure mechanisms

ABSTRACT

Investigated in this paper is the mechanical and microstructural response of specimens cut from rolled AA 6061-T6 alloy subjected to uniaxial loading at different temperatures (25, 100, 200, and 300 °C) and strain rates (10^{-4}, 10^{-3}, 10^{-2}, 10^{-1} s^{-1}). It was found that the material exhibits a strain rate and temperature dependent behavior. Microstructure observations reveal grains elongated in the loading direction with the average grain size being independent of loading conditions. However, it was observed that loading conditions influence the distribution and shape of the intermetallic phase particles. Micro cracks are observed to occur and are linked to observed damage and, consequently, decrease of ductility. Investigating the root cause of this damage mechanism reveals that particles of intermetallic phase composition are the likely sites of crack initiation. The crack-initiation mechanism at temperatures less than 200 °C is identified as crack initiation emanating from these particles while at temperatures of about 300 °C the mechanism is identified as interfacial decohesion.

© 2014 Elsevier B.V. All rights reserved.

1. Introduction

In addition to being corrosion resistant, aluminum alloys possess several attractive mechanical properties such as good specific strength and reasonable formability. By virtue of the alloying elements used, a large number of different aluminum alloys have been developed resulting in a large number of Al alloy series with each having its own set of custom properties.

The AA 6061 alloy is commonly used in the automotive industry for the production of several types of automobile parts such as wheels, panels, and structural components. In the aircraft and aerospace industries this alloy is utilized in structural components such as wings and fuselages. In the marine industry, flat-bottomed watercraft AA 6061 is used due to its light weight, high strength, and corrosion resistance even when exposed to salt water [1]. AA 6061 is an age-hardened aluminum alloy originally developed in 1935 to satisfy the need in medium-strength aluminum with high toughness and weldability [2,3]. Aluminum 6061 may be tempered into many conditions including the T6 designation.

A few recent studies reported on the mechanical and the microstructural behavior of 6061-T6 aluminum. For example, Ghahremaninezhad and Ravi-Chandar [4] studied the ductile failure behavior of AA 6061-T6 at room temperature by performing tensile tests, interrupted flat-notched tests and by observing the evolution of the microstructure at different stages of deformation. It was concluded that nucleation of damage appears in AA 6061-T6 at plastic strains of about 1.0 and that damage initiates in the form of particle fracture or decohesion at the interfaces between intermetallic phase particles and the surrounding metal. Tucker et al. [5] studied the effect of changing strain rates and stress states on the plasticity, damage and fracture of extruded AA 6061-T6. It was reported that under tension, damage in AA 6061-T6 initiates from two sources, (i) micron-scale particles and (ii) nano-scale precipitates inducing a strain sensitive damage that decrease with increasing strain rate. The impact response of AA 6061-T6 at different strain rates was investigated by Lee et al. [6] where it was concluded that strain rates influence the work hardening rate and activation volume. Using a combination of numerical and experimental techniques, Manes et al. [7] studied the strain rate effect on the behavior of AA 6061-T6 and reported on a significant increase in the strain rate effect for strain rates above 10^3 s^{-1}. The flow behavior of AA 6061 in T6 (and OA temper), under strain rates ranging from 10^{-2} to 10^5 s^{-1} was investigated by Tang et al. [8]. It was found that the precipitation-hardened AA 6061-T6 has

---

[*] Corresponding author at: Department of Mechanical Engineering, American University of Beirut, PO Box 11-0236 Beirut, Lebanon. Tel: +961 3 178 654.
E-mail address: georges.ayoub@qatar.tamu.edu (G. Ayoub).

http://dx.doi.org/10.1016/j.msea.2014.11.074
0921-5093/© 2014 Elsevier B.V. All rights reserved.

greater yield and flow strength than AA 6061-OA. Bahrami et al. [9] studied the work-hardening behavior of 6061 aluminum alloy, aged at different temperatures and durations and concluded that the dynamic recovery rates and work-hardening are lower for under-aged material than for over-aged material. They verified these results by an extended Kinetic Model Editor (KME) modeling approach through a comparison between experimental stress–strain curves and the simulation results. A number of recent articles reported [10–22] on the mechanical properties and microstructural evolution of AA 6061 having been processed by different processing techniques, namely: rolling, Equal Channel Angular Pressing (ECAP), forging friction stir processing, and different welding techniques.

For AA 6061-T6, it is important to understand the acting deformation and damage mechanisms at elevated temperatures. As such, this study aims to develop insights into the mechanical response, microstructure evolution, and mechanisms of damage leading to failure of AA 6061-T6 (commercial 61S) aluminum alloy. The study utilizes specimens placed in tension mode under various conditions of (tensile) strain rates (10^{-4}, 10^{-3}, 10^{-2}, 10^{-1} s^{-1}) and temperatures (25, 100, 200, and 300 °C). The active damage mechanisms during deformation are investigated by means of interrupted tensile tests and by analyzing the fracture surfaces of failed specimens.

2. Material, procedure, and experimental setup

The 6061 aluminum alloy is an age-hardenable alloy resulting in controllable conditions such as the desirable T6 condition. The hardening of the material, during aging, results from the dissolution, growth or coarsening of Si- and Mg-rich precipitates [2,23,24]. The mechanical properties of the AA 6061 depends on the maximum aging temperature and the heating rate that induces microstructural changes [25]. The T6 aging refers to the material heat-treated at 160 °C for 18 h and then air cooled, or the materials heated at 177 °C for 8 h and then air cooled. In addition to Si and Mg alloying elements, transition metals may and certain impurities (Fe and Mn) lead to the formation of new phase components. During casting of 6xxx alloys, among the aluminum dendrites, a variety of Fe- intermetallic phases Al–Fe, Al–Fe–Si and Al–Fe–Mn–Si are formed among aluminum dendrites. It have been reported that in the absence of chromium or manganese, the iron-rich phases are β-$Fe_2Si_2Al_9$ or α-Fe_3SiAl_{12} or a mixture of both. However, in the presence of manganese and chromium which stabilize $(Fe, Mn, Cr)_3SiAl_{12}$, the iron-rich phase will be formed into α-$(Fe, Mn)_3SiAl_{12}$ or α-$(Fe, Cr)_3SiAl_{12}$ [26,27]. In our investigation, commercial AA 6061-T6 rolled sheets with 3 mm thickness supplied by McMaster Inc. was studied. The nominal chemical composition of this alloy is provided in Table 1.

To investigate the microstructure, samples were prepared according to the standard metallographic preparation. First, specimens were cut into 10 mm^2 square pieces and then mounted in a phenolic hot working resin powder, by using a "TechPress 2™" hydraulic-pneumatic automatic mounting press. The mounted specimens are then grinded using silicon carbide abrasive paper. Here we used the 320, 600 and 1200 grits abrasive papers in consecutive steps while rotating the specimens of 90° between each step and water was used as lubricant. Finally, polishing was performed using 1 μm diamond polycrystalline suspension, followed by 0.04 μm colloidal suspension on Spec-Cloth by contra-rotating the sample until a clear, haze-free mirror surface was obtained while BlueLube was used as lubricant. Excessive force was avoided during the grinding and polishing steps to prevent the polishing compound from embedding into the aluminum matrix [4]. Once the metallographic preparation is completed, etching is performed using Weck's reagent (4% potassium permanganate ($KMnO_4$) and 1% sodium hydroxide (NaOH) in distilled water). The specimen is immersed in the etchant solution for roughly 20 s then rinsed with water, and finally rinsed with alcohol. The etchant is innocuous from a chemical point of view as it does not attack the intermetallic phases and the precipitates [28]. The microstructure is observed using a Zeiss AxioVert 40 MAT optical light microscope equipped with an ERc5s camera connected to a computer.

Table 1
Chemical composition of AA6061. ASTM. B308/B308M–02.

wt%	Al	Mg	Si	Cu	Cr	Fe	Zn	Mn	Ti	Other (each)	Other (total)
Min	95.8	0.8	0.4	0.15	0.04	–	–	–	–	–	–
Max	98.6	1.2	0.8	0.4	0.35	0.7	0.25	0.15	0.15	0.05	0.15

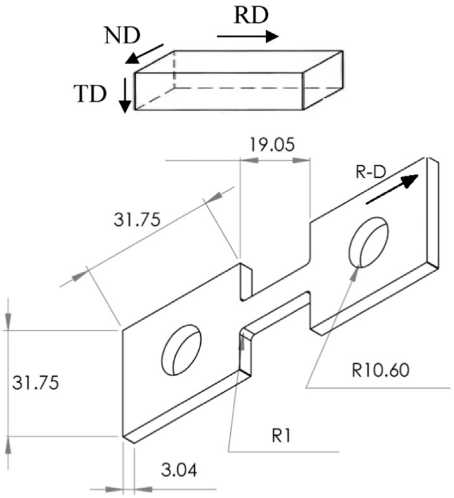

Fig. 1. Tensile test specimen geometry.

Tensile testing was performed using a computer controlled MTS Insight electromechanical testing machine with a 30 KN load cell equipped with a LBO-series Thermocraft LabTemp laboratory oven (Environmental chamber). The uniaxial tensile testing samples were prepared using a CNC machine, the samples were cut with their major axis parallel to the sheet rolling direction, and the geometry of the specimen is presented in Fig. 1. The geometry of the specimen is selected according to the ASTM E2448 - 11 (standard for superplastic tensile testing [29]).

The mechanical behavior of AA 6061-T6 was studied by performing tensile tests at different temperatures ranging from room temperature to 300 °C under strain rates of $10^{-4}\,s^{-1}$, $10^{-3}\,s^{-1}$, $10^{-2}\,s^{-1}$, and $10^{-1}\,s^{-1}$. In order to perform tests at homogenized temperature, the samples were kept in the environmental chamber for 30 min before starting the test and when the test stopped the samples were directly water quenched to preserve the microstructure. All loading conditions were repeated at least twice to verify the reproducibility of the results.

In order to examine the microstructure evolution with temperature, annealing tests were conducted on the as-received AA 6061-T6 specimens. The specimens were cut into 10 mm^2 pieces, then, placed in a Thermo-Scientific furnace for different treatment conditions.

3. Mechanical testing

The 6061-T6 aluminum alloy used in this study is a polycrystalline metal, with a face cubic centered (F.C.C) crystal unit cell.

The deformation of each of its crystals occurs by slipping which is defined to be the process by which a dislocation motion produces plastic deformation in crystalline materials. We assume that different slip systems are active during the deformation process of Al alloys, and slipping is the main deformation mechanism that occurs to carry out the plastic deformation [30]. The F.C.C unit cell has twelve {111}⟨110⟩ slip systems resulting from four {111} planes and three ⟨110⟩ directions [30,31]. The texture of this rolled aluminum can be approximated by a copper type orientation of {112} ⟨111⟩ with Euler angles values of $\varphi_1 = 90^\circ$, $\varnothing = 35^\circ$ and $\varphi_2 = 45^\circ$ and the so called S orientation type of {123} ⟨634⟩ with Euler angles of $\varphi_1 = 59^\circ$, $\varnothing = 37^\circ$ and $\varphi_2 = 63^\circ$ [32,33].

3.1. *Effect of strain rate on tensile properties*

The mechanical response of AA 6061-T6 was observed to be strain rate and temperature dependent. Fig. 2 presents the stress–strain response obtained under tensile loading for different strain rates at room temperature (Fig. 2a) and 300 °C (Fig. 2b). (The stress was calculated $\sigma = F/A$ with F being the measured load and A the current cross-sectional area. A was calculated by assuming that the material deforms at a constant volume although this assumption does not hold true after necking). At room temperature, within the range of strain rate values investigated in this paper, the material did not exhibit any significant strain rate sensitivity (Fig. 2a). The mechanical properties exhibited by the material under all strain rates show a good combination of strength (UTS=374–380 MPa) and tensile ductility (≈20%). At an elevated temperature of 300 °C, a significantly higher strain rate effect was observed (Fig. 2b), which was consistent with earlier reports in the literature [34]. The yield strength, ultimate tensile strength and strain-at-failure values decrease with decreasing strain rate. The yield strength decreases from 200 MPa for a strain rate of $10^{-1}\,s^{-1}$, to 145 MPa for a strain rate of $10^{-4}\,s^{-4}$. Under these same testing conditions, the UTS decreased from 220 MPa ($10^{-1}\,s^{-1}$) to 159 MPa ($10^{-4}\,s^{-4}$). A 20% decrease of the elongation to fracture was obtained when decreasing the strain rate from $10^{-1}\,s^{-1}$ to $10^{-4}\,s^{-1}$. In comparison to RT response, very little strain hardening was observed and it consistently decreased with decreasing strain rate; at $10^{-4}\,s^{-1}$ no strain hardening was observed in the stress–strain curve. This is likely due to the transformation of elongated iron-rich phases β-AlFeSi to rounded α-AlFeMnSi during the homogenization temperature phase [27,35,36]. Lassance et al. [36] conducted in situ SEM uniaxial tests and reported that the α- and β- phases undergo different damage mechanisms. The authors noted that as the homogenization duration is extended, the presence of α-AlFeMnSi increased accordingly, resulting in flow strength decrease.

3.2. *Effect of temperature on tensile properties*

Fig. 3 shows the stress–strain response obtained under tensile loading for different temperatures at strain rates of (a) $10^{-1}\,s^{-1}$, (b) $10^{-2}\,s^{-1}$, (c) $10^{-3}\,s^{-1}$ and (d) $10^{-4}\,s^{-1}$. It can be clearly observed that higher temperatures lead to a decrease of the yield strength and the maximum UTS. Under a constant strain rate of $10^{-1}\,s^{-1}$, it can be observed that strain-at-failure values slightly increase with increasing temperature. Strain-at-failure reached values of 0.21 and 0.18 at 300 °C and RT, respectively, as can be seen in Fig. 3a. Furthermore, UTS decreases with increasing temperature, starting from a value of 386 MPa at room temperature the UTS decreased to reach a minimum value of 220 MPa at 300 °C. A similar temperature sensitivity effect on the mechanical behavior was observed for tensile tests conducted at strain rates of $10^{-2}\,s^{-1}$, $10^{-3}\,s^{-1}$ and $10^{-4}\,s^{-1}$ (Fig. 3c and d) for temperatures ranging between RT and 200 °C. It was observed, however, that at 300 °C the value of strain-at-failure decreased to 0.20 at strain rate of $10^{-3}\,s^{-1}$ and 0.17 at strain rate of $10^{-4}\,s^{-1}$.

For yield strength, the effect of strain rate was found to be more observable at high strain rates and much larger values of yield strength was observed under all temperature conditions when strain rate increases from $10^{-4}\,s^{-1}$ to $10^{-1}\,s^{-1}$. This finding will be corroborated by the strain rate sensitivity measurements discussed later in the article. The effect of temperature on yield strength was somewhat classical for metallic alloys and the yield strength continuously decreased with increasing temperatures. It should be noted that very high tensile elongations close to superplastic behavior has never been reported in AA 6061. Especially, under the temperature range investigated in this work, the conclusion is that although the material exhibits decrease softening in flow stress with increase in temperature, the evolution of the tensile elongations is not large.

3.3. *Strain rate sensitivity*

The effect of both strain rate and temperature on the yield stress of the material could be better understood by the calculation of the strain rate sensitivity parameter m given in Eq. (1) [37]:

$$\sigma = B\dot{\varepsilon}^m \tag{1}$$

where σ is the stress, $\dot{\varepsilon}$ is the strain rate, $B = C^{-m}\exp(mQ/RT)$, C is a material constant, Q is the activation energy, R is the universal

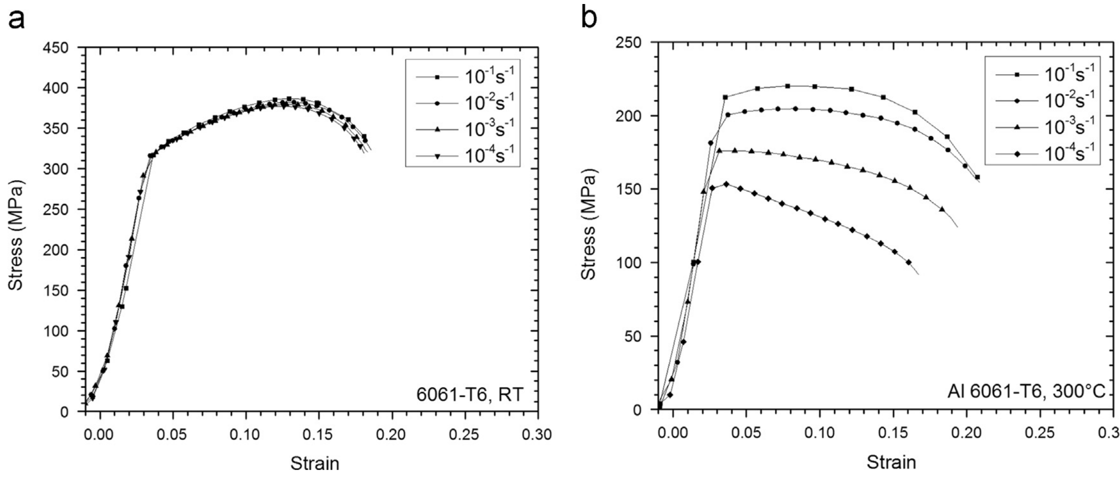

Fig. 2. Stress–strain curves response to uniaxial loading at (a) room temperature and (b) 300 °C with strain rates of 10^{-1}, 10^{-2}, 10^{-3} and 10^{-4}.

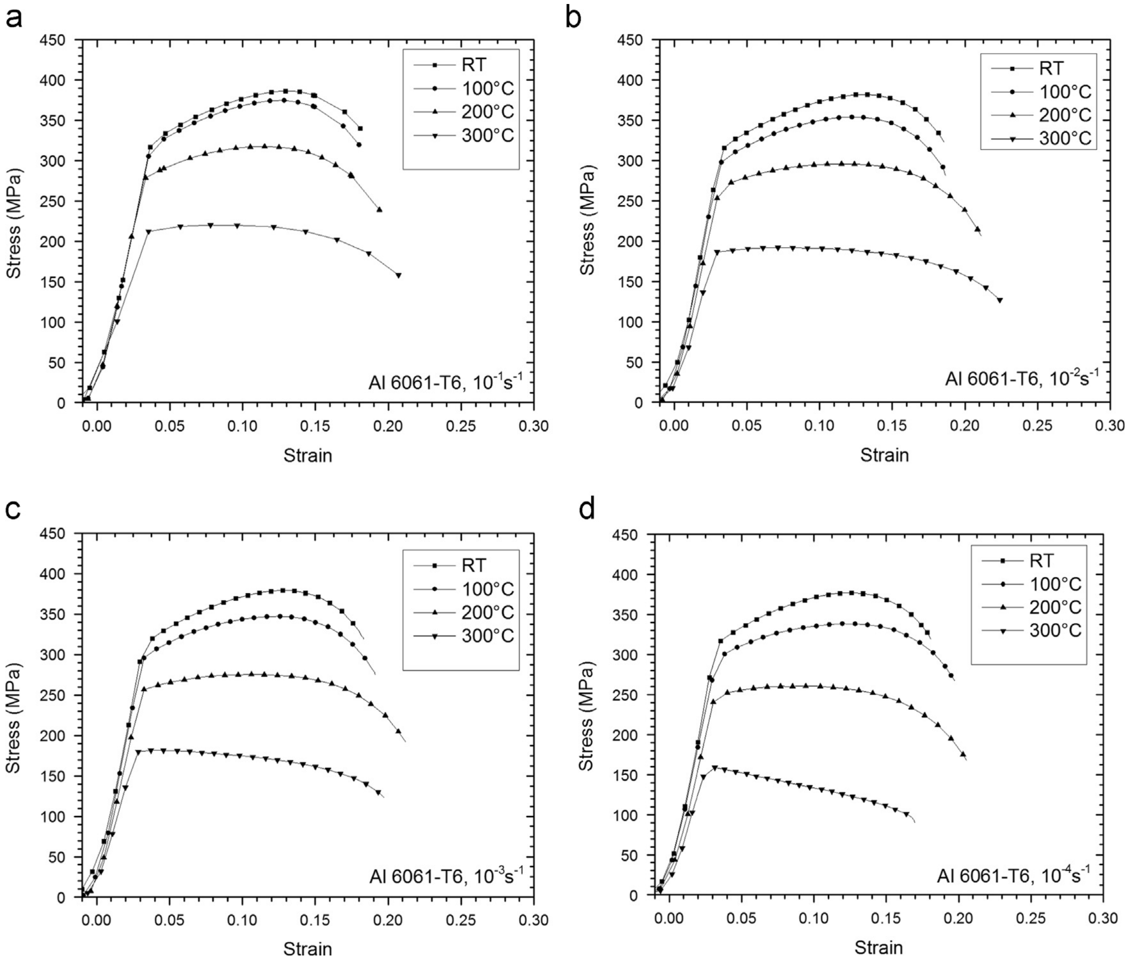

Fig. 3. Stress–strain curves response to uniaxial loading at (a) $10^{-1}\ s^{-1}$; (b) $10^{-2}\ s^{-1}$; (c): $10^{-3}\ s^{-1}$ and (d): $10^{-4}\ s^{-1}$ at temperatures of 24 °C, 100 °C, 200 °C and 300 °C.

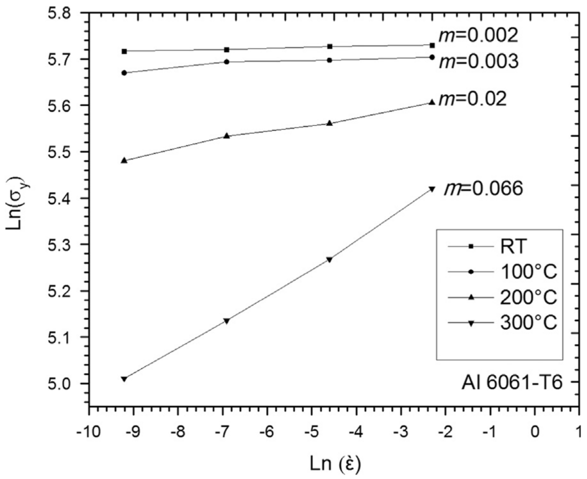

Fig. 4. Yield stress vs. strain rates at room temperature, 100 °C, 200 °C and 300 °C.

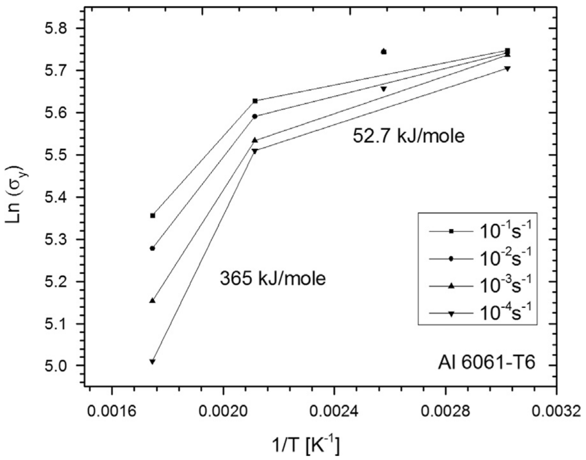

Fig. 5. Plot of Yield stress (ln scale) vs. the reciprocal of temperature (1/*T*) for various strain rates.

gas constant and *T* is the absolute temperature. The strain rate sensitivity *m* can be calculated by plotting the natural logarithm of the yield strength in function of the natural logarithm of the strain rates (Fig. 4); *m* is the slope of the resultant straight line. At room temperature, the value of the strain rate sensitivity parameter is small ($m=0.002$) reflecting the limited strain rate effect on the mechanical behavior of the AA 6061 as shown in Fig. 2. However, the strain rate sensitivity parameter increases with increasing temperature; evolving from 0.003 at 100 °C to 0.02 at 200 °C and reaching 0.066 at 300 °C. The strain rate sensitivity parameter points out the effect of strain rate on the strength of the material and the ability of the material to resist plastic instability. The small value of *m* at room temperature indicates that the critical resolved shear stress (CRSS), indicating the resistance of the material to the plastic flow, for favorably oriented independent slip system is high and therefore the materials mechanical response is insensitive to change in strain rate. In contrast, the higher value of m at 300 °C indicates a lower resistance to plastic flow, i.e. the value of CRSS at higher temperature is lower than the CRSS value at room temperature.

3.4. Activation energy

In short, the activation energy gives an insight to the deformation mechanisms occurring under given deformation conditions.

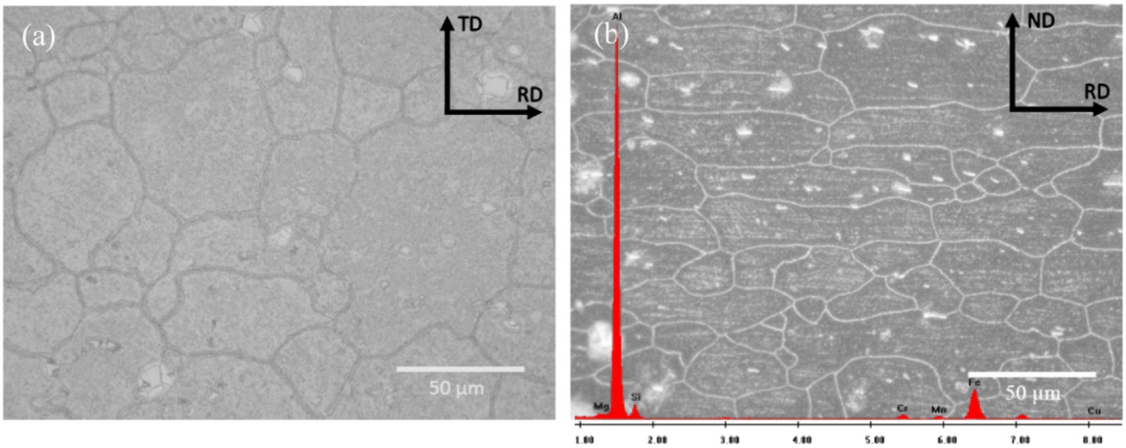

Fig. 6. Optical micrographs of microstructure of the as received AA 6061-T6 observed at the: (a) TD-RD direction and (b) ND-RD direction.

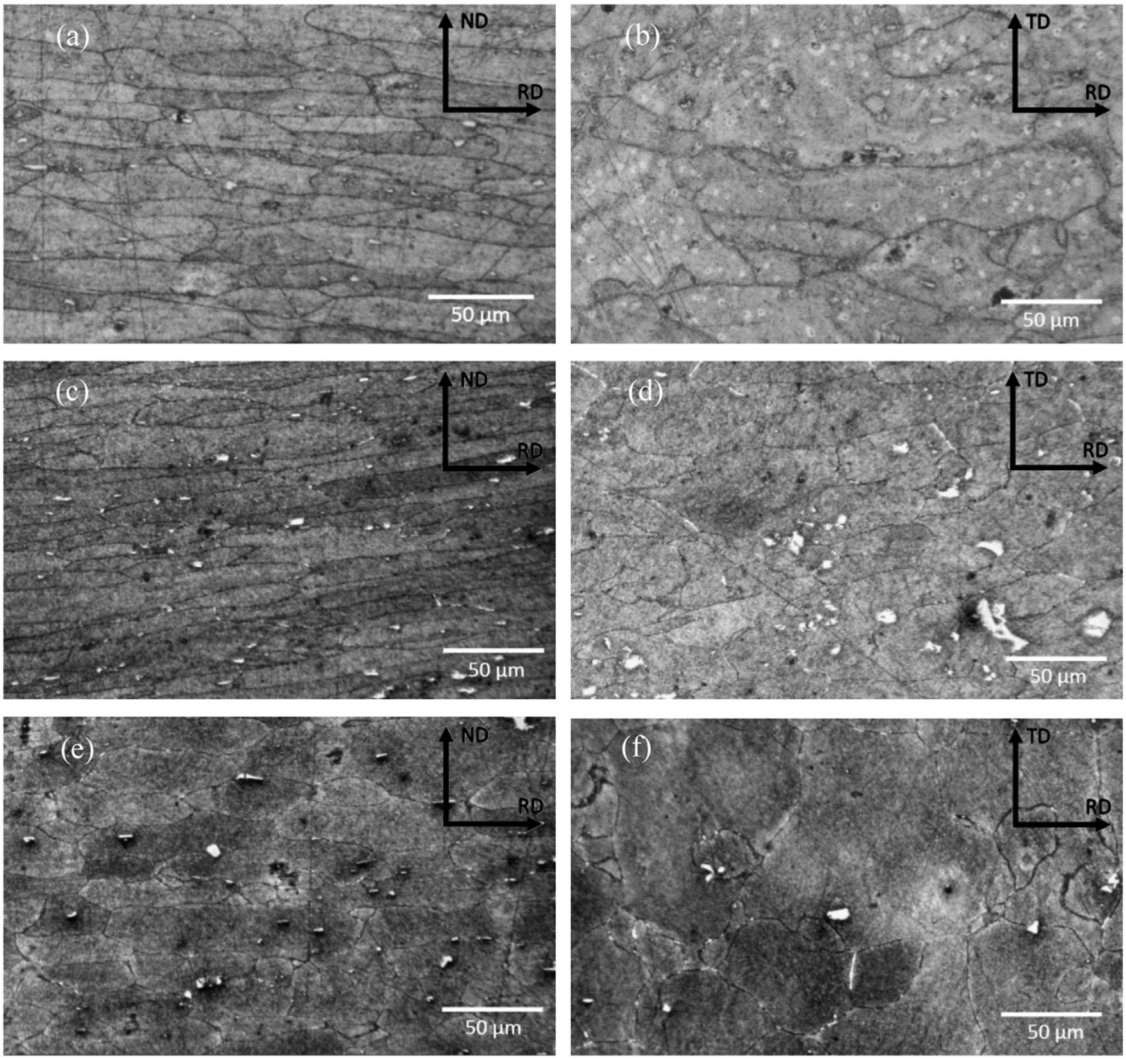

Fig. 7. Optical micrographs of microstructure of AA 6061-T6 samples deformed by uniaxial loading observed in the (a): ND-RD, loaded at RT, 10^{-1} s^{-1}; (b): TD-RD, loaded at RT, 10^{-1} s^{-1} (c) ND-RD, loaded at 300 °C, 10^{-1} s^{-1}; (d): TD-RD, loaded at 300 °C, 10^{-1} s^{-1};(e): ND-RD, loaded at 300 °C, 10^{-4} s^{-1} (f): TD-RD, loaded at 300 °C, 10^{-4} s^{-1}.

The activation energy can be calculated by plotting the values of yield strength (on natural logarithm scale) as function of the inverse of the temperature in kelvin (K^{-1}), then multiplying the obtained average slopes by the universal gas constant R and the inverse of the average strain rate sensitivity (m^{-1}) according to

$$Q_i = \frac{R}{m_i}\left(\frac{\partial \ln \sigma_y}{\partial T^{-1}}\right) \tag{2}$$

Fig. 5 is such a plot from which regions of two different slopes are revealed. The activation energy increases significantly with increasing temperature. Between room temperature and 200 °C, a region exists from which a mean (for all 4 strain rates) activation energy of Q_a=52.7 kJ/mol was calculated. This value is equal to the solute diffusion energy of chrome in aluminum ($Q_{c,Cr}$=52 kJ/mol) as reported in [38] and is lower than the dislocation core diffusion activation energy reported to be Q_c=82 kJ/mol [39].

Between 200 and 300 °C, mean (for all 4 strain rates) activation energy of Q_a=365 kJ/mole was obtained. This value is significantly higher than that of lattice self-diffusion for pure aluminum (142 kJ/mol) as reported in [40] and is comparable to activation energies for creep (ranging from 270 kJ/mol and 500 kJ/mol) as reported in [41]. It is believed that this large increase in activation energy for this alloy could partly be due to the effects of interaction between dislocations and dispersed particles or solute atoms, and may perhaps partly due to experimental scatter. It is, however, remarkable to note that even with such high values of activation energy, which would otherwise ensure activation of grain boundary sliding, leading to enhanced plastic flow, was not observed to occur in this material. The slip systems that were operative at room temperature were perhaps aided by easy flow of dislocations, but over-all the precipitates present at grain boundaries and at grain interior appeared to have been effective in reducing dislocation motion.

4. Microstructure observation

The microstructure of the as received AA 6061-T6 is observed in two planes as showed in Fig. 6: the Rolling Direction and the Normal to the rolling Direction plane (ND-RD) and the Rolling Direction and the Transverse to the rolling Direction plane (TD-RD). Grain size analyses are performed on microstructure taken from different zones of the specimen and then by using the grain size analysis module; AxioVision software. The grains in the ND-RD plane have elliptic shape due to rolling while they are round shaped in the TD-RD plane. The mean grain size is found to be equal to 39 μm and 25 μm in the transverse and the normal planes respectively. The iron-rich phases and the magnesium silicide particles (Mg_2Si) were clearly observed even after etching. Energy-Dispersive X-ray Spectroscopy (EDS) analysis was used to verified that the gray particles are the iron-rich phase (Fe, Mn, $Cr)_3SiAl_{12}$ (Fig. 6b). Therefore, it can be concluded that the iron-rich phases are distributed between the grain boundaries and within the grains.

4.1. Microstructure observation of deformed specimens

In order to develop better understanding of the material's behavior, the microstructure of the deformed material at different loading conditions was studied in this section. Fig. 7 presents the microstructure of the deformed AA 6061-T6 specimens with micrographs taken near the fracture zone and the observation is conducted in two planes: TD-RD and ND-RD. Fig. 7a and b presents the microstructure of specimen tested at room temperature and strain rate of 10^{-1} s^{-1}, it is observed that the grains are significantly elongated in the tensile loading direction i.e. RD. However, it can be observed from Fig. 7c and d that the grains are more elongated for the specimen tested at 300 °C and deformed at the

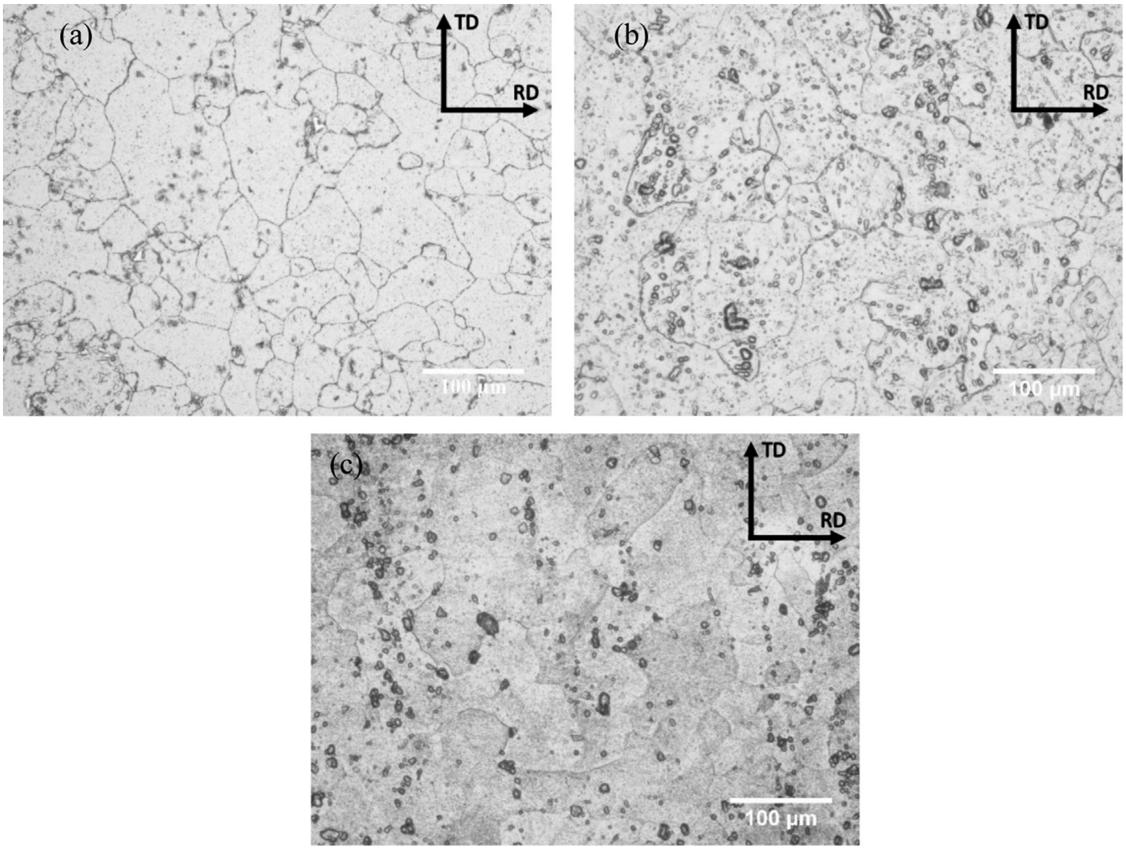

Fig. 8. Optical micrographs showing the microstructure of annealed AA 6061-T6 at (a) 300 °C for 50 min (b) 450 °C for 8 h and (c) 580 °C for 8 h.

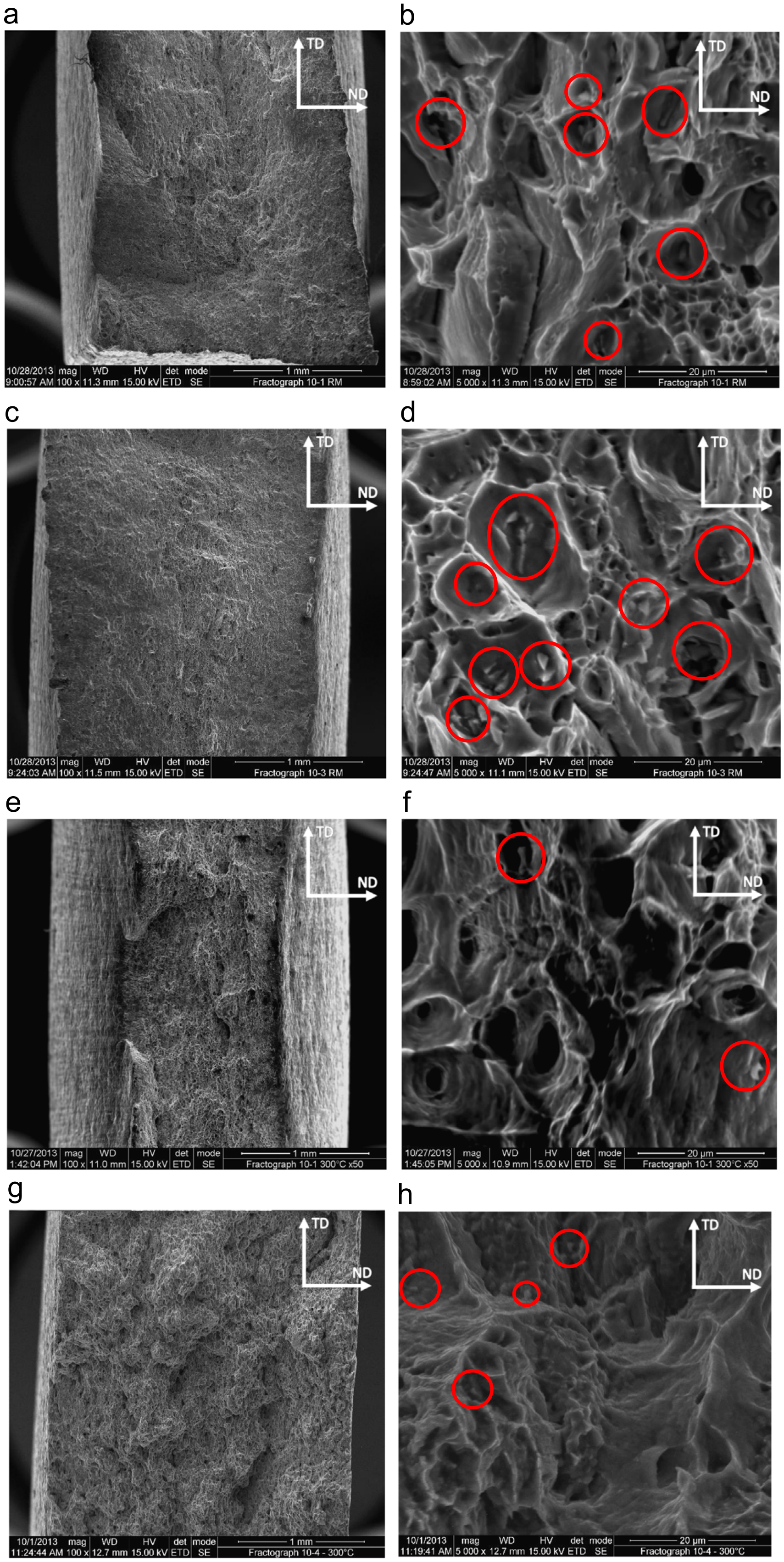

Fig. 9. SEM fractographs of uniaxially loaded samples, (a) and (b) at room temperature under strain rate of 10^{-1} s^{-1}, (c) and (d): at room temperature under strain rate of 10^{-3} s^{-1} (e) and (f): at 300 °C under strain rate of 10^{-1} s^{-1}, (g) and (h): at 300 °C under strain rate of 10^{-4} s^{-1}. (For interpretation of the references to color in this figure, the reader is referred to the web version of this article.)

same strain rate. This observation can be explained by the higher strain-at-failure obtained in the specimen at 300 °C as shown in Fig. 3a. Also, the grains are observed to be less elongated for specimen tested at 300 °C and strain rate of $10^{-4}\,s^{-1}$. Furthermore, the shape of the grains is quite different from the previous cases – more rounded grains can be seen in Fig. 7e and f. A grain size analysis was performed for the different testing conditions. No significant grain growth was found, as the mean grain size remained 25 µm and 39 µm in the ND-RD and TD-RD planes respectively for the different testing conditions. Moreover, it was observed that the precipitates migrated and they were more perceptible at the grain boundaries, it was concluded that these observations could explain the limited grain growth observed in the 6061-T6 aluminum alloy [38]. Since there was no significant grain growth observed under the deformation range investigated in this work, it can point out that the main deformation mechanism is slip. It goes to suggest that a better formability response, i.e. large elevated temperature tensile ductility, may be obtained at significant higher temperatures through the activation of other deformation mechanisms. Therefore, it could possibly enable the activation of grain boundary sliding and grain fragmentation, and enhance the dislocation motion as the precipitates would grow and globalize. The evolution of the microstructure with heat treatment was checked in the following paragraph.

4.2. Annealing tests

Fig. 8 shows the microstructure of AA 6061-T6 annealed samples at 300 °C ± 3 °C for 50 min (Fig. 8a), at 450° ± 3 °C for 8 h (Fig. 8b) and at 580 °C ± 3 °C for 8 h (Fig. 8c). The average grain size diameter was found to be 41 µm for 300 °C ± 3 °C for 50 min. This annealing condition was performed in order to confirm that no significant grain growth takes place at this temperature. Average grain size of 50 µm and 61 µm was found for condition of 450° ± 3 °C for 8 h and for condition of 580 °C ± 3 °C for 8 h, respectively. As annealing temperature is increased, it is observed that the dispersion and coarsening of magnesium silicide (Mg_2Si) particles become more abundant in agreement with the findings in [42].

4.3. Fractography analyses

Fracture surfaces were examined by Scanning Electron Microscopy (SEM). Fig. 9 presents SEM fractographs of uniaxially loaded samples at room temperature and 300 °C under strain rates of $10^{-1}\,s^{-1}$, $10^{-3}\,s^{-1}$, $10^{-4}\,s^{-1}$. It can be observed that the fracture surface presented in Fig. 9e compared to the other four conditions supported the largest strain-at-failure values. The existence of coalesced micro-voids and microscopic dimples in all the SEM micrographs of Fig. 9, confirm that the AA 6061-T6 exhibits a ductile behavior [8]. Under the strain rate of $10^{-4}\,s^{-1}$ and 300 °C, the estimate mean size and the depth of these microscopic dimples are small compared to the one observed at strain rate of $10^{-1}\,s^{-1}$. Iron-rich phases were supposedly observed at the bottom of some micro-voids and highlighted by red circles in Fig. 9 [4]. These iron-rich particles were especially perceivable in the fracture surfaces of the samples deformed at room temperature (Fig. 9b and d). The microscopic dimples depth are observed to be bigger in the fracture surfaces of the samples deformed at 300 °C at a strain rate of $10^{-1}\,s^{-1}$ (Fig. 9f), which can explain the reason why intermetallic phases are less perceivable. In other words, the depth of the microscopic dimples may be used to give an approximate estimate of the ductility of a metallic alloy [43]. Indeed, the samples with higher strain-at-failure had relatively deep estimated microscopic dimples (Fig. 9f) and samples with lower strain-at-failure have relatively shallow estimated microscopic dimples (Fig. 9h).

4.4. Work of fracture

Values of the work to fracture were calculated in order to develop a deeper insight into the evolution of the deformation and damage mechanisms under variable loading conditions. The work of fracture W_e is calculated as the area under the stress–strain curve at given loading condition. The values of work of fracture at temperature or $W_e(T)$ are plotted as function of temperature for different strain rates in Fig. 10a. It is observed that the work to fracture decrease with increasing temperature and decreasing strain rate. At room temperature the work to fracture was found to be fairly consistent i.e. 60 MPa, showed negligible strain rate sensitivity. This however began to decrease gradually with increasing temperature, and at 300 °C it dropped to 42 MPa under strain rate of $10^{-1}\,s^{-1}$ and to 21 MPa under strain rate of $10^{-4}\,s^{-1}$.

Fig. 10b presents the work to fracture $W_e(\dot{\varepsilon})$ of AA 6061-T6 as a function of the natural logarithm of the strain rate for different temperatures. It is observed that at RT and 100 °C the work to fracture is almost constant with evolving strain rate. However, for 200 °C and 300 °C, the work to fracture is observed to decrease with decreasing strain rate. The work to fracture reaches its minimal value for uniaxial test performed at 300 °C at a strain rate of $10^{-4}\,s^{-1}$.

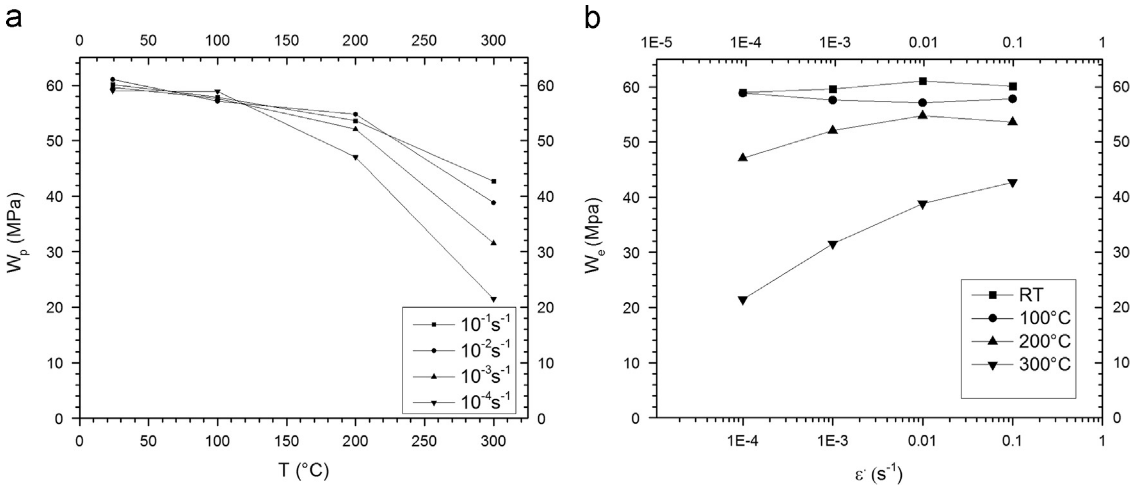

Fig. 10. Plots of (a) work of fracture vs. temperature and (b) work of fracture vs. strain rate.

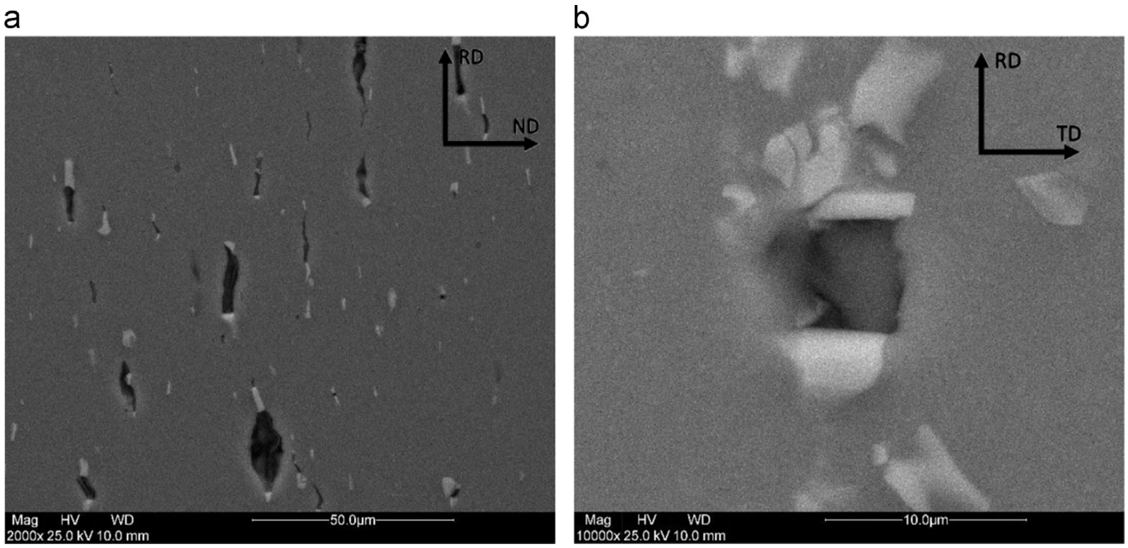

Fig. 11. SEM analysis of interrupted uniaxial tensile test of AA6061-T6 at $10^{-3}\,s^{-1}$ and 200 °C, observed in the (a) RD-ND plane and (b) RD-TD plane.

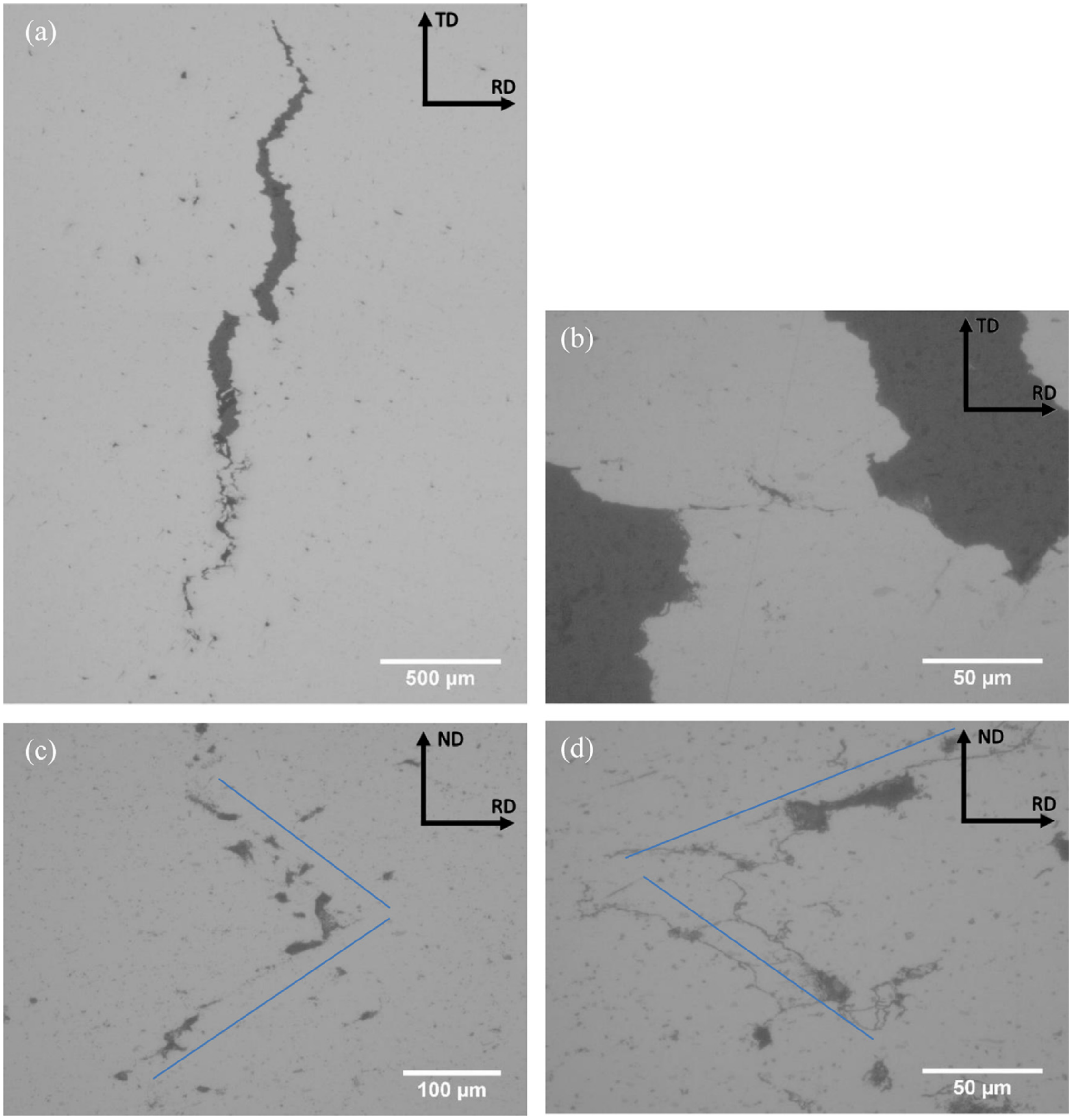

Fig. 12. Optical micrographs of crack initiations of interrupted test at 300 °C, (a) and (b) $10^{-3}\,s^{-1}$ in TD-RD plan, (c): $10^{-3}\,s^{-1}$ in ND-RD plan, (d) $10^{-4}\,s^{-1}$ in ND-RD plan.

The yield stress and the strain-at-failure are the main parameters affected by the strain rate and the temperature evolution. We had observed that increasing strain rate results in increasing the yield stress and hence contributes to increase in the work to fracture. However, increasing strain rate resulted in decreasing the strain-at-failure for tests conducted at RT and 100 °C and in increasing the strain-at-failure for tests conducted at 200 °C and 300 °C. A competition between the yield stress and the strain-at-failure sensitivity to strain rate and temperature will determine the evolution of work to fracture. The evolutions of $W_e(T)$ and $W_e(\dot{\varepsilon})$ point out that the increase in the yield stress with increasing strain rate and decreasing temperature is not countered by the strain-at-failure sensitivity. In the purpose to identify the damage mechanisms controlling the fracture behavior of the AA 6061 T6, the cracks initiation and evolution are tracked in samples loaded at 200 °C and 300 °C.

4.5. Damage mechanisms

It is widely recognized that plastic deformation of ductile metals and their alloys is limited by the void nucleation and growth and associated coalescence rates [44]. Therefore, in order to identify the damage mechanisms that control the fracture of the AA 6061-T6 specimens loaded at 200 °C and 300 °C, crack initiation and subsequent evolution was tracked. Fig. 11 shows SEM micrographs of a specimen taken from an interrupted (specimen at the instant of initiation of strain-to-failure) test. The particular sample was uniaxially loaded at strain rate of $10^{-3}\,s^{-1}$ and temperature of 200 °C. Cracks were observed between broken second-phase particles or apparently iron-rich phases (white particles). These micro-voids were observed in the RD-ND and RD-TD planes but mainly in the RD-ND plane. Similar observations have been reported by [4] on specimen tested at room temperature. The Iron rich phase particles are locations for stress concentration that leads to cracks initiation that was evidenced by the void growth parallel to the loading direction [45,46]. These observations could give an explanation to the presence of some iron-rich phases in the bottom of the microvoids observed in the fractograph surfaces (Fig. 9).

Fig. 12 shows optical microscope micrographs of specimen surfaces subjected to tensile tests, conducted at 300 °C, and interrupted at strains of 0.2 and 0.16 for test strain rates of $10^{-3}\,s^{-1}$ and $10^{-4}\,s^{-1}$, respectively. These micrographs were taken in the middle of the samples; they show that the cracks leading to fracture propagates in the necked region. These cracks propagated parallel to each other and coalesce in localized shear bands formed in the thinned ligament between neighboring voids as observed in Fig. 12(b). It can be noticed from Fig. 12 that in the TD-RD plane the cracks are propagating in the transverse direction (TD) (Fig. 12a, b). However, in the RD-ND plane a number of cracks are scattered all over the micrograph, slightly propagating along the rolling direction (RD), and coalescing in localized shear bands

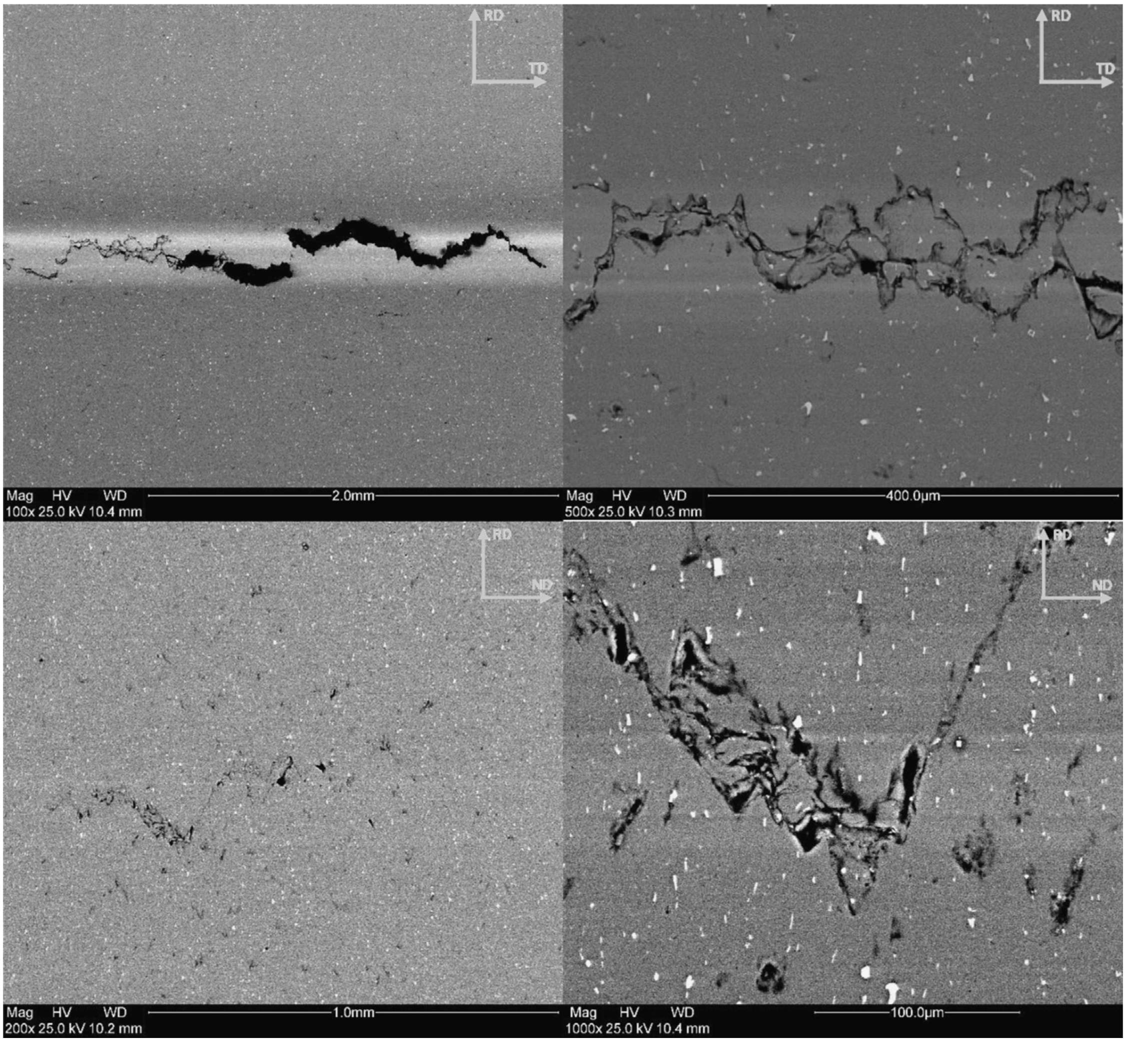

Fig. 13. SEM micrographs of an interrupted tensile test at 300 °C, (a) and (b) $10^{-3}\,s^{-1}$ in TD-RD plan, (c) and (d): $10^{-3}\,s^{-1}$ in ND-RD plan.

formed between two neighboring cracks (Fig. 12c, d). The propagation of cracks parallel to the transverse direction (TD) and the coalescence of cracks in the RD-ND plane will lead to a macroscopic crack propagating with an α angle from the normal direction (ND) in the RD-ND plane that will lead to the catastrophic failure of the sample.

Fig. 13 presents SEM micrographs of tensile samples tested at 300 °C and 10^{-3} s^{-1} strain rate but interrupted at the instant of initiation of strain-to-failure. Similar observation as in that in Fig. 12 can be made where cracks propagate parallel to the transverse direction (TD) and coalesce in the RD-ND plane. It can be observed that the intermetallic phase particles do not appear to have fractured and that cracks have developed adjacent to the particles. In contrast with those at 200 °C and RT, the cracks the 300 °C appear to have initiated at the intermetallic phase particles which leave us to conclude that the interfacial decohesion is the main crack initiation mechanism at this temperature.

5. Conclusions

The mechanical behavior and the associated microstructural evolution of AA 6061-T6 were studied under uniaxial loading tests performed at different combinations of strain rates (10^{-4}, 10^{-3}, 10^{-2}, 10^{-1} s^{-1}) and temperatures (25, 100, 200, and 300 °C). The yield stress and the ultimate tensile strength were observed to increase with increasing strain rates and decreasing temperatures. Maximum values of strain-at-failure were found to increase with increasing temperature and decreasing strain rate for tests performed at room temperature and at 100 °C. By contrast, the maximum value of strain-at-failure was found to decrease with increasing temperature and decreasing strain rate for tests performed at 200 °C and 300 °C. Microstructure observations revealed that, although the grains exhibited elongation in the loading direction, the average grain size did not proportionally evolve with the different loading conditions.

Significant dispersion and coarsening of magnesium silicide (Mg_2Si) particles with increasing temperature was observed. This observation was further confirmed through heat treatment (annealing) at different temperatures and durations. However, the average grain size seemed to increase at elevated temperatures and for longer durations. Analysis of the fractured surfaces of failed specimens confirmed the ductile behavior nature of AA 6061-T6 as coalesced micro-voids and microscopic dimples were observed. To track the evolution of damage in the AA 6061-T6 specimens, the microstructure was observed for samples subjected to interrupted tests. It was found that the intermetallic phase particles are the likely sites of crack initiation. The mechanism responsible for crack initiation seems to change depending on temperature: initiation by particle fracture at temperatures at 25 °C and up to 200 °C and by interfacial decohesion at 300 °C. With further deformation, cracks were observed to propagate perpendicular to the rolling direction (RD). Subsequent coalescence of cracks occurred in the RD-ND plane and resulted in observable macroscopic cracks propagating at an angle, α, from the normal direction (ND) in the RD-ND plane and ultimately leading to the catastrophic failure of the sample.

Acknowledgment

This presentation was made possible by NPRP Grant # 4-1063-2-397 from Qatar National Research Fund (A member of Qatar Foundation). The statements made herein are solely the responsibility of the authors.

References

[1] H. Agarwal, A.M. Gokhale, S. Graham, M.F. Horstemeyer, Mater. Sci. Eng.: A 341 (2003) 35–42.
[2] G.A. Edwards, K. Stiller, G.L. Dunlop, Appl. Surf. Sci. 76/77 (1994) 219–255.
[3] R. Sanders Jr., JOM 53 (2001) 21–25.
[4] A. Ghahremaninezhad, K. Ravi-Chandar, Int. J. Fract. 174 (2012) 177–202.
[5] M.T. Tucker, M.F. Horstemeyer, W.R. Whittington, K.N. Solanki, P.M. Gullett, Mech. Mater. 42 (2010) 895–907.
[6] W.-S. Lee, J.-C. Shyu, S.-T. Chiou, Scr. Mater. 42 (1999) 51–56.
[7] A. Manes, L. Peroni, M. Scapin, M. Giglio, Procedia Eng. 10 (2011) 3477–3482.
[8] X. Tang, D. Li, V. Prakash, J.J. Lewandowski, Mater. Sci. Technol. 27 (2011) 13–20.
[9] A. Bahrami, A. Miroux, J. Sietsma, Metall. Mater. Trans. A 44 (2013) 2409–2417.
[10] P.N. Rao, D. Singh, R. Jayaganthan, Mater. Des. 56 (2014) 97–104.
[11] J.A. Vargas, J.E. Torres, J.A. Pacheco, R.J. Hernandez, Mater. Des. 52 (2013) 556–564.
[12] P. Nageswara Rao, R. Jayaganthan, Mater. Des. 39 (2012) 226–233.
[13] R.R. Ambriz, G. Barrera, R. García, V.H. López, Mater. Des. 31 (2010) 2978–2986.
[14] A. Masoudian, A. Tahaei, A. Shakiba, F. Sharifianjazi, J.A. Mohandesi, Trans. Nonferrous Met. Soc. China 24 (2014) 1317–1322.
[15] E. Tan, A.A. Kibar, C.H. Gür, Mater. Charact. 62 (2011) 391–397.
[16] S.-Y. Chang, K.-S. Lee, S.-H. Choi, D. Hyuk Shin, J. Alloys Compd. 354 (2003) 216–220.
[17] R.R. Ambriz, G. Barrera, R. García, V.H. López, Mater. Des. 30 (2009) 2446–2453.
[18] S. Venukumar, S. Yalagi, S. Muthukumaran, Trans. Nonferrous Met. Soc. China 23 (2013) 2833–2842.
[19] J.K. Kim, H.K. Kim, J.W. Park, W.J. Kim, Scr. Mater. 53 (2005) 1207–1211.
[20] M.W. Fu, Y.W. Tham, H.H. Hng, K.B. Lim, Mater. Sci. Eng.: A 526 (2009) 84–92.
[21] F. Ozturk, A. Sisman, S. Toros, S. Kilic, R.C. Picu, Mater. Des. 31 (2010) 972–975.
[22] M.R. Shankar, S. Chandrasekar, A.H. King, W.D. Compton, Acta Mater. 53 (2005) 4781–4793.
[23] I. Dutta, S.M. Allen, J. Mater. Sci. Lett. 10 (1991) 323–326.
[24] C. Ravi, C. Wolverton, Acta Mater. 52 (2004) 4213–4227.
[25] D. Maisonnette, M. Suery, D. Nelias, P. Chaudet, T. Epicier, Mater. Sci. Eng.: A 528 (2011) 2718–2724.
[26] J.E. Hatch, A. Association, A.S.f. Metals, Aluminum: Properties and Physical Metallurgy, American Society for Metals, 1984.
[27] G.M. Nowotnik, J. Sieniawski, M. Wierzbińska, Arch. Mater. Sci. Eng. 28 (2007) 69–76.
[28] T. Zwieg, Prakt. Metallogr. 38 (2004) 3–6.
[29] A.K. Rodriguez, G. Kridli, G. Ayoub, H. Zbib, JMEP 22 (2013) 3115–3125.
[30] D. Hull, D.J. Bacon, Introduction to Dislocations. Fifth Edition, 2011.
[31] L. Polmear, Light Alloys: From Traditional Alloys to Nanocrystals, 2006.
[32] C.-H. Choi, D. Lee, Metall. Mater. Trans. A 28 (1997) 2217–2222.
[33] K. Kashihara, H. Inagaki, Mater. Trans. 50 (2009) 528–536.
[34] L. Blaz, E. Evangelista, Mater. Sci. Eng.: A 207 (1996) 195–201.
[35] N.C.W. Kuijpers, F.J. Vermolen, C. Vuik, P.T.G. Koenis, K.E. Nilsen, S.v.d. Zwaag, Mater. Sci. Eng.: A 394 (2005) 9–19.
[36] D. Lassance, D. Fabrègue, F. Delannay, T. Pardoen, Prog. Mater. Sci. 52 (2007) 62–129.
[37] M.F. Shi, D.J. Meuleman, JMEP 4 (1995) 321–333.
[38] A.V. Kazantzis, Z.G. Chen, J.Th.M. DeHosson, J. Mater. Sci. 48 (2013) 7399–7408.
[39] R.W. Balluffi, Phys. Status Solidi (b) 42 (1970) 11–34.
[40] H.J. Frost, Deformation-mechanism maps: The Plasticity and Creep of Metals and Ceramics, Oxford Oxfordshire New York: Pergamon Press, Oxford [Oxfordshire] New York, 1982.
[41] M.A. Meyers, K.K. Chawla, Mechanical Behavior of Materials, second edition, 2009.
[42] Y. Lee, Y. Kwon, J. Lee, C. Park, S. Kim, Mater. Sci. Eng.: A 362 (2003) 187–191.
[43] H. Bethge, J. Heydenreich, Electron Microscopy in Solid State Physics, Elsevier, Amsterdam, 1987.
[44] R.D. Thomson, J.W. Hancock, Int. J. Fract. 26 (1984) 99–112.
[45] G.E. Dieter, Mechanical Metallurgy, DI Metric Edition, 1986.
[46] D. Zhu, B. Mobasher, S. Rajan, P. Peralta, J. Eng. Mech. 137 (2011) 669–679.